Journal of Materials Chemistry C

ROYAL SOCIETY OF CHEMISTRY

PAPER

View Article Online
View Journal | View Issue

Cite this: J. Mater. Chem. C, 2024, 12, 7605

Chemically driven dimensionality modulation of hybrid tin(II) halide perovskite microcrystals†

Raúl I. Sánchez-Alarcón, [a] Omar E. Solís,[a] María Cristina Momblona-Rincon, [a] Teresa S. Ripolles, *[a] Juan P. Martínez-Pastor,[a] Rafael Abargues *[a] and Pablo P. Boix *[ab]

The lattice arrangement of lead-free perovskites can be altered by synthesis parameters such as concentration, temperature, choice of solvents, and the length of monovalent cations. This effect, often described as dimensionality modulation, can be exploited to develop new materials with better optical properties than their three-dimensional counterpart. This work explores the versatility of the hot-injection synthesis for obtaining 2-thiopheneethylammonium (TEA^+) based tin halide perovskite microcrystals. The dimensionality of TEA-based tin bromide perovskite microcrystals can be modulated through changes in the TEA concentration, giving rise to the formation of highly luminescent 0D-TEA_4SnBr_6 and low-emissive 2D-TEA_2SnBr_4 microplates. In contrast, 0D-[TEASnCl$_3$][TEACl] and 2D-TEA_2SnI_4 are thermodynamically preferred as main products when using the chloride and iodide analogues, respectively, limiting the dimensional versatility. It is noteworthy that 0D-TEA_4SnBr_6 shows the highest PLQY from the low dimensional TEA tin halide family (PLQY = 75% in thin-film) owing to a more confined configuration based on isolated $[SnBr_6]^{4-}$ octahedra moieties separated by TEA^+ cations, being attractive for optoelectronic applications.

Received 16th February 2024,
Accepted 2nd May 2024

DOI: 10.1039/d4tc00623b

rsc.li/materials-c

Introduction

Lead halide perovskites show promising properties for semiconductor-based applications, such as efficient energy conversion in solar cells.[1] However, one of their major drawbacks is the toxicity of lead, a key component usually present in most efficient compositions. Researchers are actively exploring alternative materials to replace lead in perovskites, aiming to mitigate environmental and health concerns. This has become a key area of research with the aim of developing environmentally friendly and sustainable technologies. The most common approach to form lead-free perovskites is to replace Pb(II) with Sn(II). Since both of them present the same valence electron configuration (ns^2sp^2), the resulting perovskites can offer similar properties, maintaining the perovskite structure and optoelectronic behaviour, such as high charge carrier mobility, high light absorption properties, and small exciton binding energy.[2] However, tin-based perovskites exhibit lower stability than their lead-containing counterparts.[3] Even though Sn and Pb present multiple oxidation states, tin forms more commonly Sn(II) and Sn(IV) ions, while lead is often found as Pb(II). The reason for this is attributed to the lanthanide contraction effect in Pb by the presence of $4f^{14}$ electrons in its electronic configuration. Conversely, Sn lacks lanthanide shrinkage, leading to easy loss of all valence electrons, and consequently, forming Sn^{4+} ions.[4]

Reducing the dimensionality of perovskite materials by disaggregation of inorganic moieties with bulky organic cations is a promising approach to mitigate the Sn-based perovskite stability issues.[5] For example, in two dimensional perovskites, 2D, layered perovskite moieties are hydrogen bonded with voluminous organic spacers, which are self-assembled by van der Waals forces and π-stacking. If layers of 3D perovskites are stuck within the voluminous organic spacers, the physical properties depend on the thickness of inorganic perovskite moieties, being possible to tune the exciton binding energy and band gap of the resulting materials.[6] On the other hand, if the density of bulky organic cations is high enough to separate the structure on individual polyhedron moieties, these conduce to the formation of zero-dimensional perovskite structures, 0D.[7]

This bulky organic layer can act as a protection from external agents, increasing environmental stability. It also leads to a higher confinement of bounded excitons than their three-dimensional material counterpart,[8] which can be advantageous

[a] Instituto de Ciencia de los Materiales-Universidad de Valencia, Catedrático José Beltrán, 2, 46071, Valencia, Spain. E-mail: teresa.ripolles@uv.es, rafael.abargues@uv.es, Pablo.P.Boix@itq.upv.es
[b] Instituto de Tecnología Química, Instituto de Tecnología Química, Universitat Politècnica València-Consejo Superior de Investigaciones Científicas, Av. dels Tarongers, 46022 València, Spain

† Electronic supplementary information (ESI) available. See DOI: https://doi.org/10.1039/d4tc00623b

for light emitting applications.[9] From the fundamental point of view, manipulating the dimensionality of tin-based perovskites can also impact their bandgap, carrier mobility, and other electronic properties due to the spatial confinement of charge carriers. For example, 2D tin halide perovskites present radiative recombination of free excitons by increasing the exciton 2D binding energy.[10,11] On the other hand, 0D tin halide perovskites exhibit radiative recombination of self-trapped excitons (STEs) at energy levels originating from the optical distortion of Sn–X bonds.[12,13] In particular, STEs refer to the strong electron (exciton) phonon coupling when a soft lattice is distorted upon photoexcitation.[14] Interestingly, 0D-tin halide perovskites show higher PLQYs, better environmental stability, higher Stokes shift, and a major exciton binding energy compared to their 2D and 3D counterparts.[13,15,16]

However, inorganic and hybrid tin halide compounds can adopt multiple dimensionalities depending strongly on the polyhedron type (owing to the high coordination number of Sn(II) ions), inorganic or organic cations, oxidation number, and preparation conditions (pH, temperature, atmosphere, *etc*).[17,18] For example, zero-dimensional tetrabutylammonium (TBAC) tin(II) chloride could be obtained under acidic conditions with stable pyramidal $[SnCl_3]^-$ anions.[19] If the monovalent cation is changed to Cs^+, 3D-$CsSnCl_3$ with $[SnCl_6]^{4-}$ octahedrons is stable at high temperature because $5s^2$ orbitals hybridize with $5p_z$, resulting in hybrid orbitals with the same energy as that of np halogen orbitals.[18,20] It should be mentioned that the octahedral tin chloride configuration is also stable for Sn(IV) ions.[21] Different inorganic and organic tin(II/IV) halide compounds and dimensionalities are summarized in Table 1.

Thus, lead-free low-dimensional tin(II) halide perovskites are attracting scientific attention owing to their unique combination of interesting physical properties and lower toxicity.[31] They show great potential as visible light emitters on optoelectronic devices[32] as well as for enhancing the performance of photovoltaic devices.[33] Among multiple organic cations tested on low-dimensional hybrid metal halide perovskites, 2-thiopheneethylammonium (TEA^+) has drawn attention as a heteroatomic organic spacer and a passivating agent for lead iodide perovskites, with a stable power conversion efficiency (PCE) of 18.75% for 1000 h[34,35] when used in solar cells. Concerning tin-based perovskites, the synthesis of 2D-TEA_2SnI_4 has been reported at different scales, from nanocrystals[36] and thin films[37] to single crystals,[38] showing a PLQY around 19% for nanodisks in solution prepared by the LARP method[36] and 23% for thin films prepared using the antisolvent approach.[37] However, to the best of our knowledge, the synthesis and characterization of TEA-based Sn(II) chloride and bromide remain unexplored.

The dimensionality of perovskite nanocrystals synthesized by the hot injection method can be modulated by means of changes in the precursor concentrations.[39–41] Dimensional modulation improves the optical properties of lead-free perovskites and their PLQY owing to the separation and distortion of metal halide octahedrons with lone electron pair ns^2.[42] For instance, Cs-oleate solution precursor concentration is a cornerstone parameter that determines whether 0D-Cs_4SnBr_6 or 3D-$CsSnBr_3$ nanocrystals are obtained.[43,44] Appropriate dimensionality manipulation of lead-free perovskites expands the range of these less toxic materials with a full gamut of wavelength emission depending on the type of inorganic moiety and organic cation. Therefore, the hot injection approach could be re-imagined as a controlled method to achieve high luminescent perovskite nanostructures.[39,43]

Here, we report the synthesis of 2D and 0D TEA-based Sn(II) halide perovskite microplates by the hot injection method. The control of the [TEA]/[Sn^{2+}] ratio for the bromide-based perovskite adjusts the resulting perovskite dimensionality from 2D to 0D. The PLQY was strongly affected by this factor, ranging from 0.1% for 2D-TEA_2SnBr_4 to 75% for orange emitting 0D-TEA_4SnBr_6. Interestingly, TEA/Sn(II)-driven dimensionality control only takes place with TEA-based tin(II) bromide derivatives. Conversely, the reaction between $SnCl_2$ and SnI_2 with TEA provides main products pure 0D-[$TEASnCl_3$][TEACl] and 2D-TEA_2SnI_4 microplates, respectively.

Materials and methods

Chemicals

Mesitylene (97% Pure) and iodotrimethylsilane (TMSI, 95–97% stabilized) were purchased from Thermo Scientific.

Table 1 Dimensionality of different inorganic and hybrid tin halide compounds

Cation	Compound	Polyhedral unit	Dimensionality	Ref.
$TBAC^+$	(TBAC)$SnCl_3$	$[SnCl_3]^-$	0D	19
R/*S*-α-PEA^+	*R*/*S*-α-PEA SnX_3, (X = Cl, Br)	Distorted $[SnX_6]$	1D	22
MA^+, FA^+	$ASnI_3$ (A = MA^+, FA^+)	$[SnI_6]^{4-}$	3D	23
PEA^+	PEA_2SnI_4	$[SnI_6]^{4-}$	2D	24
H_4BAPP^{3+}	$H_4BAPPSnX_5$ (X = Cl, Br)	$[SnX_5]^{3-}$	0D	25
$C_7H_8N_3^+$	$(C_7H_8N_3)_4SnBr_6$	$[SnBr_6]^{4-}$	0D	26
Cs^+	$CsSn_2Br_5$	$[Sn_2Br_5]^-$	1D	27
DAO^{2+}	$DAOSn_2I_6$	$[Sn_2I_6]^{2-}$	1D	28
IPA^+	μ-$[IPA]_3Sn_2I_7$	$[Sn_2I_7]^{3-}$	2D	29
$(CH_3)_3S^+$	$[(CH_3)_3S]_2SnCl_6{\cdot}H_2O$	$[SnCl_6]^{2-}$	0D	21,27
Cs^+, MA^+, FA^+	A_2SnI_6	$[SnI_6]^{2-}$	Undefined	30

List of acronyms. $TBCA^+$ = tetrabutylammonium; *R*/*S*-α-PEA^+ = *R*/*S*-α-phenethylammonium; MA^+ = methylammonium; FA^+ = formamidinium; H_4BAPP = 1,4-bis(3ammoniumpropyl)piperazinium; $C_7H_8N_3^+$ = 2-amino benzimidazolium; Cs^+ = cesium; DAO^{2+} = 1,8-octyldiammonium; IPA^+: isopropylammonium; $(CH_3)_3S^+$ = trimethyl sulfonium.

Bromotrimethylsilane (TMSBr, 98%) and *n*-octane were acquired from Acros Organics. Chlorotrimethylsilane (TMSCl, 98%), trioctylphosphine (TOP, 97%), tin(II) ethylhexanoate (95–100%), *n*-hexane and oleic acid (OLAC, technical grade of 90%) were obtained from Sigma Aldrich. 2-Thiopheneethylamine (TEA, > 98%) was purchased from TCI Chemicals. All the chemicals were used without further purification.

Experimental procedure

Synthesis of SnX_2-TOP precursor solution. In a standard procedure, 1 mL of tin(II) 2-ethylhexanoate and 2 mL TOP were mixed in a 25 mL round bottom flask and degassed in a vacuum with magnetic stirring for 45 min at room temperature. After that, the atmosphere was changed by nitrogen flux, and three mmol of TMSX was injected, keeping a molar ratio of [TMSX]/[Sn^{2+}] of 2. Finally, the SnX_2-TOP solution was stored under a nitrogen atmosphere for further use.

Synthesis of 0D-[$TEASnCl_3$][TEACl], 0D-TEA_4SnBr_6 and 2D-TEA_2SnX_4 (X = Br, I) microplates. In a 100 mL 3-neck round bottom flask, 20 mL of mesitylene and 1 mL of oleic acid were degassed under vacuum for 1 h at room temperature. Subsequently, the SnX_2-TOP solution was injected into the reaction system at room temperature to obtain a precursor solution with a nominal concentration of 0.12 M of SnX_2-TOP. After that, the temperature was increased until 160 °C, and TEA was injected. Different [TEA]/[Sn^{2+}] molar ratios between 0.3 and 4 were tested to modulate the dimensionality of the final product. After 5 s, the reaction mixture was chilled in an ice bath with continuous magnetic stirring. TEA-based tin(II) halide microplates were isolated by centrifugation and washed three times with n-hexane. The final product was re-dispersed in *n*-octane and stored in a glovebox for further characterisation. All proceedings (synthesis and purification) were carried out under normal atmospheric conditions of moisture and oxygen.

Characterisation

X-ray diffraction (XRD) diffractograms were measured with an Empyrean diffractometer from PANalytical and the measurements were conducted in the range of $2\theta = 4°–60°$ with a 2θ step of 0.026° and using a Cu target as an X-ray source (Kα Cu radiation, λ = 0.15406 nm). For XRD measurements, 10 μm films were prepared by drop-casting lead-free microcrystal dispersions on *n*-octane over 0.5 cm × 0.5 cm glass substrates and drying at room-temperature under an inert atmosphere.

^{1}H and ^{13}C nuclear magnetic resonance (NMR) spectra in the liquid phase for 0D-TEA_4SnBr_6 and 2D-TEA_2SnX_4 (X = Br, I) were recorded with a Bruker AV400 spectrometer, with an Oxford Magnet of 400 MHz (9.4 T). ^{1}H and ^{13}C NMR spectra are reported in ppm (δ) relative to the chemical shift of solvent residual signals for DMSO-d_6 at 2.51 ppm and 39.99 ppm, respectively.

^{13}C and ^{119}Sn magic angle solid state nuclear magnetic resonance (MAS-NMR) spectra of 0D-[$TEASnCl_3$][TEACl], 0D-TEA_4SnBr_6, and 2D-TEA_2SnX_4 (X = Br, I) were measured with a Bruker Advance III 400 WB spectrometer, with an ultra-shielded Widemouth magnet (89 mm), 400 MHz (9.4T), two RF channels and high-power amplifiers for solid-state experiments. For ^{119}Sn MAS-NMR spectra measurements, the SnO powder sample was used as a reference. On the other hand, for ^{13}C and ^{119}Sn MAS-NMR and liquid state NMR, perovskite microcrystals were isolated from n-octane suspension by centrifugation and dried under an inert atmosphere overnight. ^{119}Sn MAS-NMR spectra of 0D-[$TEASnCl_3$][TEACl] were measured at different spinning rates (8 kHz and 10 kHz).

Transmission electron microscopy (TEM) images were acquired from a Hitachi HT7800 microscope with a high-resolution filament of LaB_6 with an acceleration voltage of 100 kV. TEA-based tin(II) halide microcrystal suspensions in n-octane were dropped on Cu/C TEM grids.

Energy-dispersive X-ray spectroscopy (EDS) microanalysis was performed using an Oxford Ultim Max 170 detector monitored with Aztec software coupled to a SCIOS2 FESEM microscope from Thermo Scientific. For these measurements, TEA-based tin(II) halide microcrystals were deposited on Si substrates, and sample borders were coated with Ag paste.

Photoluminescence (PL) and photoluminescence excitation (PLE) measurements were conducted in an FLS1000 spectrophotometer from Edinburgh Instruments. A xenon lamp (Xe2) was used as an excitation source. PL spectra were recorded with a PMT-980 detector from Edinburgh Instruments. PL and PLE spectra were measured with a dwell time of 1 s and a wavelength step of 1 nm. The PL quantum yield (PLQY) was measured with an integrating sphere coupled to an FLS1000 spectrophotometer from Edinburgh Instruments. TEA based tin(II) halide microcrystal films were prepared over 0.25 cm^2 quartz substrates by drop cast deposition to measure PLE and PL spectra and PLQY.

Results and discussion

The hot injection method was employed to synthesize 0D-TEA_4SnBr_6 and 2D-TEA_2SnBr_4 microcrystals by adjusting the precursor concentration, as detailed in the Experimental section, with [TEA]/[Sn^{2+}] ratios of 1 and 0.3, respectively. Thin films fabricated from 2D-TEA_2SnBr_4 microcrystals exhibited flakes with an average particle size of 7.66 μm ± 5.2 μm, and a mean thickness of 280 nm (Fig. 1a–c). On the other hand, quasi-rectangular plates with a length of ~32± 8 μm and a thickness of ~3.55 μm were predominantly observed on 0D-TEA_4SnBr_6 thin films (Fig. 1d–f).

Fig. 2a shows the XRD diffractograms of TEA-based Sn(II) bromide perovskite films for different [TEA]/[Sn^{2+}] ratios. From [TEA]/[Sn^{2+}] < 0.5, the XRD diffractogram shows the multiple reflections peaks at 2θ of 5.62°, 11.32°, 17.02°, 22.78°, 28.64° and 34.56°. These reflections are spaced apart by a 2θ interval of 5.7°, as expected from a Ruddlesden–Popper phase for pure 2D TEA_2SnBr_4.[36] Additionally, EDS analysis (Table S1, ESI†) reveals that Br/Sn and S/Sn atomic ratios are in good agreement with the expected stoichiometry. As the [TEA]/[Sn^{2+}] ratio increases, isolated metal halide octahedra $[SnBr_6]^{4-}$ or clusters are generated. From [TEA]/[Sn^{2+}] > 0.5, new non-periodically XRD

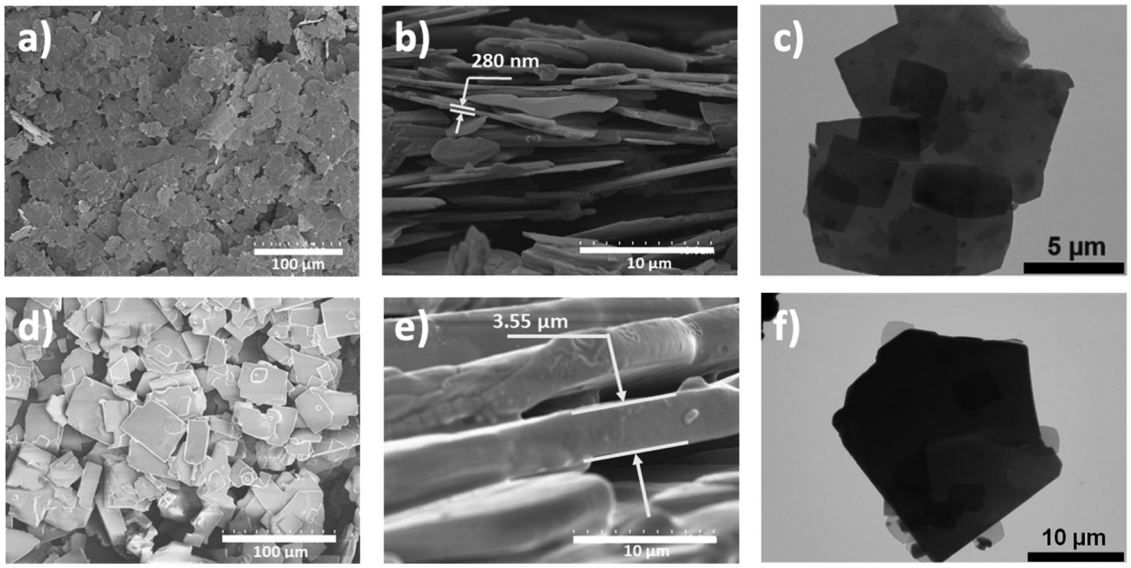

Fig. 1 Top-view SEM (a) and (d), cross-sectional SEM (b) and (e) and TEM images (c) and (f) of 2D-TEA_2SnBr_4 (a)–(c) and 0D-TEA_4SnBr_6 (d)–(f) microcrystals.

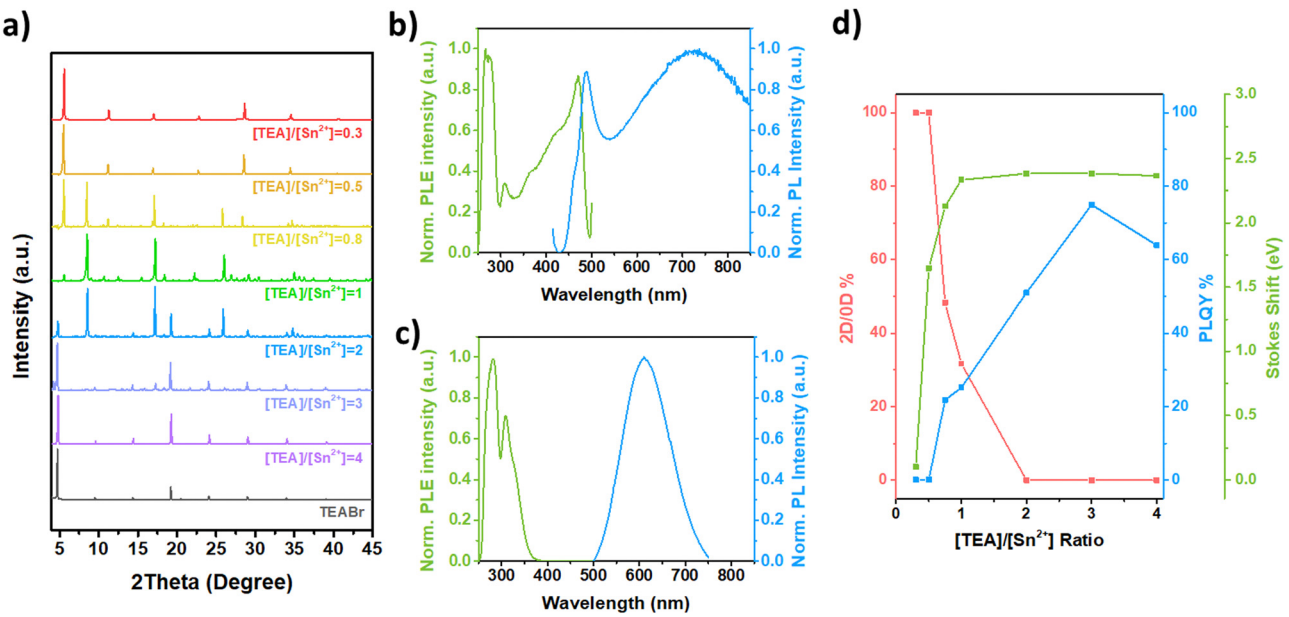

Fig. 2 (a) XRD patterns of 2D-TEA_2SnBr_4 and 0D-TEA_4SnBr_6 samples synthesized at different molar ratios [TEA]/[Sn^{2+}]; PL and PLE spectra of: (b) 2D-TEA_2SnBr_4 and (c) 0D-TEA_4SnBr_6; (d) 2D/0D ratio (red line), PLQY % (blue line) and Stokes shift (green line) as a function of [TEA]/[Sn^{2+}] ratio. PLQYs of 2D-TEA_2SnBr_4 and 0D-TEA_4SnBr_6 thin film samples were measured at a fixed wavelength of 280 nm.

peaks are observed at 8.52°, 17.13°, 18.23° and 25.84°, which are attributed to 0D-TEA_4SnBr_6. Atomic percentages of Br are higher than those measured for 2D-TEA_2SnBr_4 microplates (Table S1, ESI†), which supports the proposed chemical formula.

Concurrently, the increase of TEA molarities results in a decrease in the formation of the 2D-TEA_2SnBr_4 phase. From [TEA]/[Sn^{2+}] > 2, the diffractograms reveal only reflection peaks of 0D-TEA_4SnBr_6 along with those of pure TEABr at 2θ values of 4.5°, 9°, 14°, 19°, 24°, 29° and 34°. As expected, 0D-TEA_4SnBr_6 reflection peaks do not exhibit the same periodic ordering observed in the 2D-TEA_2SnBr_4.

The differences between 2D-TEA_2SnBr_4 and 0D-TEA_4SnBr_6 crystal phases and band structures also generate remarkable differences in their optical properties. PL emission and PL excitation (PLE) spectra of TEA–Sn(II) bromide films synthesized at different molar ratios are shown in Fig. S1 (ESI†). In particular, the [TEA]/[Sn^{2+}] ratio of 0.5, for 2D-TEA_2SnBr_4 films,

is represented in Fig. 2b. Its PL spectra can be deconvoluted into two bands; one sharp band at 470 nm, and another broader band centered at 730 nm. The shape of the PL emission bands is similar to that reported for 2D-PEA_2PbI_4,[45] thus mainly determined by the radiative recombination of free excitons. Additionally, the PLE spectrum exhibits a sharp band at 470 nm. From the spectral difference in the position of the band maximum of the PL and PLE spectra, we measured the Stokes shift energy, which is around 113 meV. The sharp PL and PLE bands shown in Fig. 2b, along with the high order observed in XRD, may be associated with the synthesis of lamellar-like microcrystals. These structures consist of intercalated layers comprising $[SnBr_6]^{4-}$ octahedra and organic layers of TEA^+ cations, as reported for 2D-TEA_2SnI_4 nanocrystals and thin films.[46] In contrast, the PL emission and PLE spectra of 0D-TEA_4SnBr_6 films synthesized with a [TEA]/[Sn^{2+}] ratio of 3 are displayed in Fig. 2c. When the perovskite was exposed to UV light (wavelength of 282 nm), 0D-TEA_4SnBr_6 exhibited a PL spectrum characterized by a band centered at 610 nm and an FWHM of 130 nm. The PLE spectrum shows two sharp bands with a maximum at 282 nm and 310 nm. From PL and PLE spectra, we measured a strong Stokes shift of 2.38 eV, which is attributed to the radiative recombination of self-trapped excitons.[47,48]

The larger bandgaps and Stokes shifts when transitioning from the 2D to 0D TEA-based Sn bromide perovskite are attributed to a reduction of the orbital overlap between $[SnX_6]^{4-}$ octahedra as the 0D phase becomes more predominant with increasing [TEA]/[Sn^{2+}] ratio. This occurs because TEA^+ cations separate the $[SnBr_6]^{4-}$ octahedra of 2D layers to form isolated $[SnBr_6]^{4-}$ octahedra. This results in a higher exciton binding energy, lower carrier mobility, and increased stability. The isolated structure of 0D perovskites also imparts a strong quantum confinement effect, contributing to a higher PL emission compared to that of higher dimensionality.

Fig. 2d shows the 0D/2D phase ratio, PLQY, and Stokes shift of TEA-based Sn(II) bromide perovskite films depending on the [TEA]/[Sn^{2+}] molar ratio. To estimate the phase ratio between 2D and 0D materials, we used eqn (1):

$$R_{2D/0D} = \frac{A_{2D}}{A_{0D} + A_{2D}} \quad (1)$$

where $R_{0D/2D}$ is the 2D/0D phase ratio in the sample, A_{0D} and A_{2D} are the integrated area under XRD peaks (Fig. 2a) corresponding to 2D-TEA_2SnBr_4 ($2\theta_{2D}$ = 5.62°, 11.32°, 17.02°, 22.78°, 28.64° and 34.56°) and 0D-TEA_4SnBr_6 ($2\theta_{0D}$ = 8.52°, 17.13°, 18.23° and 25.84°), respectively. In the transition ratios, as the presence of 0D phase increases, we observe a dramatic increase in the PLQY from 0.15% for the pure 2D perovskite to 75% at λ_{ex} = 280 nm and 62.75% at λ_{ex} = 280 nm for a [TEA]/[Sn^{2+}] ratio of 3 (with a slight PLQY reduction at higher ratios). Moreover, the Stokes shift increases noticeably (Fig. 1d) from 113 meV from 2D-TEA_2SnBr_4 to a maximum of 2.36 eV for 0D-TEA_4SnBr_6.

Based on our experimental results, the growth of 0D-TEA_4SnBr_6 is strongly influenced by the isolation of $[SnBr_6]^{4-}$ octahedra layers from the 2D-TEA_2SnBr_4 material onto individual clusters resulting from the increase of TEA^+ concentration. Also, the growth of 0D-TEA_4SnBr_6 is not influenced by coupling with mesitylene or oleic acid molecules as it is the case of the phenethylammonium tin(II) bromide perovskite, and thus the separation of inorganic moieties is influenced mostly by the increment in the TEA^+ concentration.[49] As a consequence,

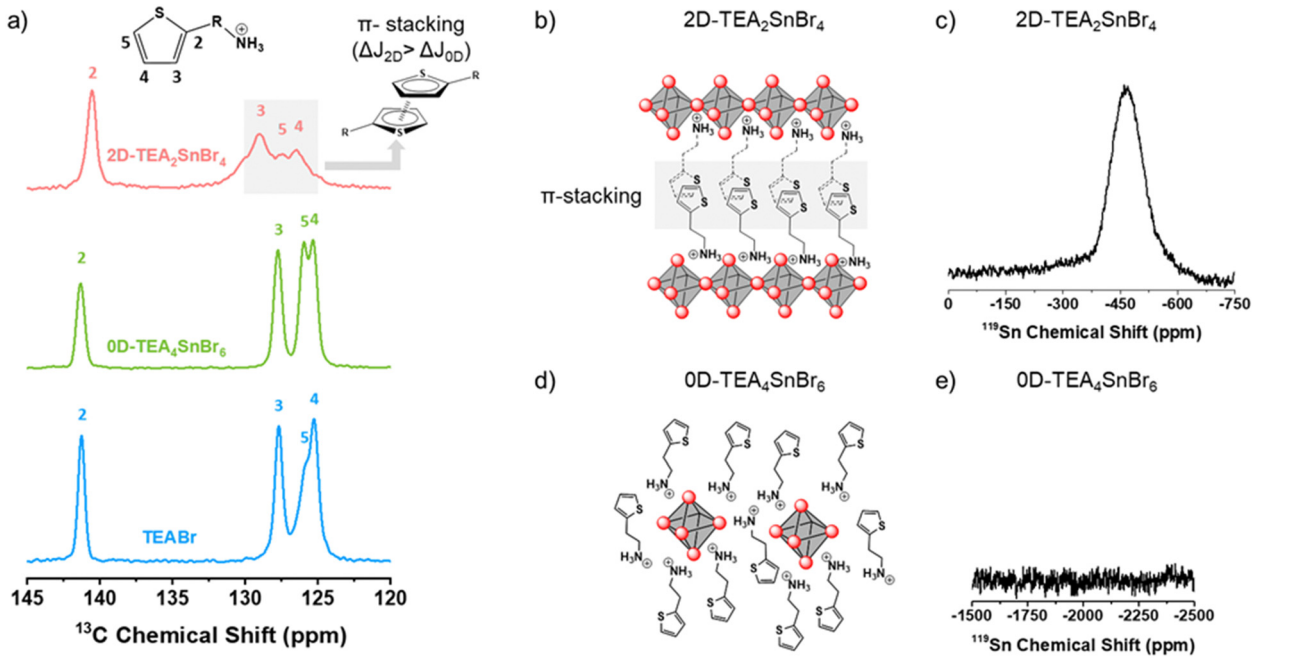

Fig. 3 (a) ^{13}C MAS-NMR spectra of TEABr, 0D-TEA_4SnBr_6, and 2D-TEA_2SnBr_4 powders. Crystalline structures and ^{119}Sn NMR of (b) and (c) 2D-TEA_2SnBr_4 and (d) and (e) 0D-TEA_4SnBr_6.

highly luminescent 0D-TEA_4SnBr_6 microcrystals can be synthesized by controlling the concentration of TEA.[50]

A qualitative magic angle solid state (MAS) NMR analysis was carried out to investigate the local environment and chemical bonding of carbon (^{13}C) and tin (^{119}Sn) nuclei in solid-state materials (Fig. 3). 2D-TEA_2SnBr_4 and 0D-TEA_4SnBr_6 are compared with TEABr to determine the internal structure of low dimensional TEA-based Sn(II) bromide perovskites.

The ^{13}C NMR spectra of 2D-TEA_2SnBr_4, 0D-TEA_4SnBr_6, and TEABr are shown in Fig. 3a. A set of four signals, ranging from 145 to 120 ppm, has been ascribed to the aromatic carbons of TEA^+. J_1, J_2, and J_3 signals observed in 2D-TEA_2SnBr_4 are shifted to a higher field (ΔJ = 1.21 ppm) than those of 0D-TEA_4SnBr_6 (ΔJ = 0.41 ppm) in comparison with TEABr. A characteristic signature of π-stacking interactions often manifests in changes to signal intensity and peak broadening in NMR spectra. The π-stacking interactions among aromatic rings lead to dynamic processes, causing an exchange between stacked and unstacked conformations. This equilibrium results in broader peaks in the NMR spectra due to variations in the chemical environments experienced by the interacting nuclei.

At a low [TEA]/[Sn^{2+}] ratio, TEA^+ can be distributed between layers of $[SnBr_6]^{4-}$ octahedra, leading to the formation of a 2D tin bromide perovskite. In this structure, $[SnBr_6]^{4-}$ octahedra are interconnected through four corner-sharing, creating 2D perovskite monolayers. Under these conditions, we can assume that thiophene rings self-assemble by π–π stacking interaction between thiophenes of adjacent 2D perovskite monolayers in 2D-TEA_2SnBr_4.[51] This combination of structural features contributes to the unique properties and characteristics of the resulting material.[52] Conversely, when the [TEA]/[Sn^{2+}] ratio is high, the TEA^+ cations form a surrounding layer around individual $[SnBr_6]^{4-}$ octahedra, resulting in a lack of interconnection between the octahedra. The high [TEA]/[Sn^{2+}] ratio influences the structural organization, and the isolation between $[SnBr_6]^{4-}$ octahedra enables their strong quantum confinement effect, which has implications for the properties of the material, such as radiative recombination by self-trapped excitons.[44] The TEA^+ cations randomly distributed around the $[SnBr_6]^{4-}$ octahedra reduce the π stacking interaction. As a result, the chemical shifts of aromatic carbons observed in 0D-TEA_4SnBr_6 are very similar to those of TEABr.[53]

Regarding the ^{119}Sn MAS-NMR spectra, 2D-TEA_2SnBr_4 (Fig. 3d and Fig. S2, ESI†) shows two different signals at −465 ppm and −1983 ppm assigned to Sn(II) and Sn(IV) respectively,[20] with a lower intensity for the latter. In the case of 0D-TEA_4SnBr_6, no significant signal was observed between −1000 and −2000 ppm. This is fully aligned with the better ambient stability displayed by the 0D-TEA_4SnBr_6 compared to its bidimensional counterpart.

Optical and structural properties of 0D-[TEASnCl$_3$][TEACl] and 2D-TEA_2SnI_4 microcrystals

It is key to understand if a similar approach can be carried out to selectively control the dimensionality of the expanded TEA-based Sn(II) halide family. Microcrystals based on chloride can be synthetized with different [TEA]/[Sn^{2+}] ratios. The XRD patterns of TEA-based Sn(II) chloride films (Fig. 4a) displayed reflection peaks at 8.63°, 17.26°, 18.09°, and 26.03° for ratios ranging from 0.125 to 1. These peaks show slight shifts compared to those of 0D-TEA_4SnBr_6 (2θ values of 8.52°, 17.13°, 18.23°, and 25.84°) (Fig. 2a), which is attributed to a decrease in the lattice parameters resulting from the use of chloride.[54] For [TEA]/[Sn^{2+}] ratios between 2 and 4, XRD is dominated by the reflections of the TEACl salt, which is in excess. Noticeably, PL spectra show a broad emission band between 450 and 850 nm,

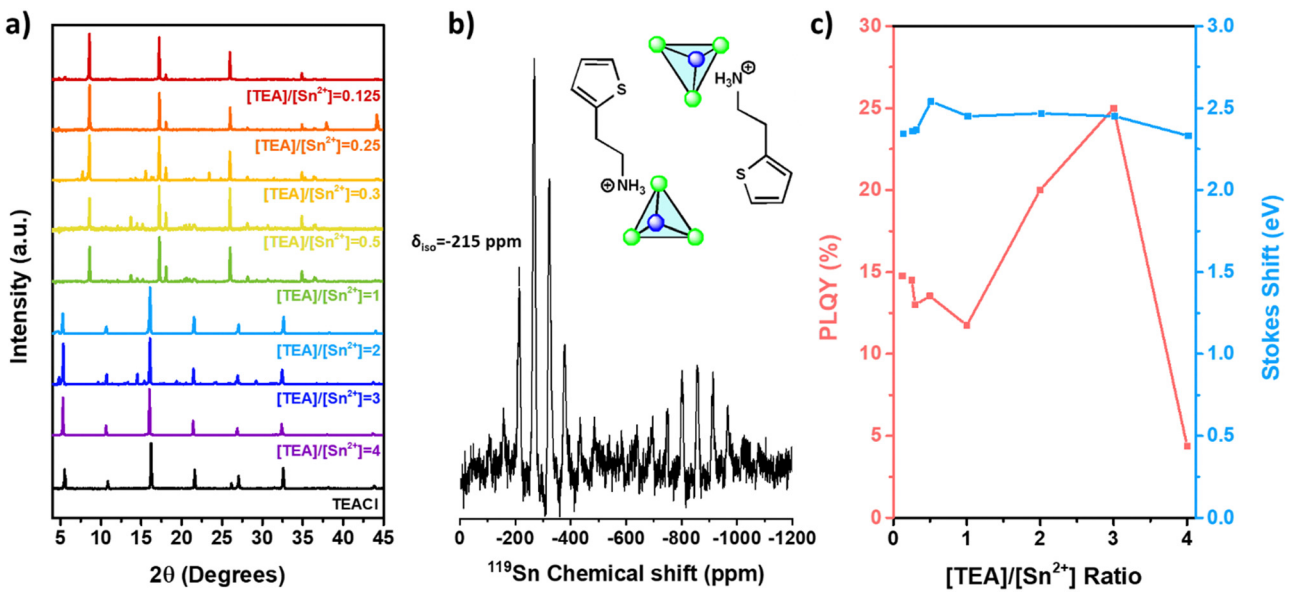

Fig. 4 (a) XRD patterns, (b) ^{119}Sn MAS-NMR spectra measured at room temperature (Inset: probable crystalline structure) and (c) variation of the PLQY and Stokes shift of 0D-[TEASnCl$_3$][TEACl] microcrystals as a function of the molar ratio [TEA]/[Sn^{2+}].

with a high Stokes shift energy of 2.38 eV for all the [TEA]/[Sn^{2+}] ratios tested (Fig. S3, ESI†). This is a characteristic fingerprint of 0D TEA-based Sn(II) chloride.[47,48] However, in contrast to the high values obtained for the 0D Br-based materials, the PLQY increases slightly from 14.77% (microcrystals thin films) for samples synthesized under Sn(II) rich conditions ([TEA]/[Sn^{2+}] = 0.125) to a maximum of 25% at high TEA concentrations ([TEA]/[Sn^{2+}] = 3). These XRD patterns and emission properties indicate that only 0D-TEA-based Sn(II) chloride can be synthesized regardless of the [TEA]/[Sn^{2+}] ratio.

Interestingly, the ^{119}Sn MAS-NMR spectrum of TEA-based Sn(II) chloride microcrystals (Fig. 4b) revealed a series of peaks between −100 ppm and −800 ppm related to the chemical shift anisotropy (CSA) effect (δ_{iso} = −215 ppm) of Sn(II). This can be attributed to the formation of $[SnCl_3]^-$ trigonal pyramids instead of $[SnCl_6]^{4-}$ octahedra.[55] To complement ^{119}Sn MAS-NMR measurements, EDS analysis shows that Br/Sn and S/Sn atomic ratios are 4.4 and 2.5, respectively. This may initially suggest a stoichiometry similar to the 2D counterpart. However, the CSA effect depicted in Fig. 4b indicates the presence of a low symmetry site for Sn(II). Therefore, we propose a chemical formula of 0D-[$TEASnCl_3$] [TEACl]. A similar stoichiometry has been reported for different 0D Sn(II) chloride perovskites (A = Cs^+, MA^+, FA^+, $(CH_3)_3S^+$, $C_6H_{22}N_4Cl_3^+$, and TBA^+).[19,20,56–58] Some authors have reported the formation of 0D-Cs_2SnCl_6 with high symmetry $[SnCl_6]^{2-}$ octahedra, which showed a single signal on ^{119}Sn NMR around −708 ppm.[20,56,59–61] Additionally, other reports suggest a possible phase transition between $[SnCl_3]^-$ trigonal pyramids to $[SnCl_6]^{4-}$ octahedra for Cs-based Sn(II) chloride, with a characteristic NMR signal at −561 ppm observed after annealing the sample above 500 °C under vacuum.[56,62] In our case, distinguishing between $[SnCl_6]^{4-}$ (from phase transition) and $[SnCl_6]^{2-}$ (produced by oxidation of Sn(II) ions) is not directly accessible due to the CSA effect observed in Fig. 4b. Moreover, the signals observed in Fig. S4 (ESI†) change in intensity at different spinning rates in NMR experiments, yet the chemical shifts are the same. As a consequence, we can conclude that TEA-based Sn(II) chloride microcrystals are synthesized as a 0D material with well-defined $[SnCl_3]^-$ pyramidal anions. EDS analysis (Table S1, ESI†) is in good agreement with the proposed stoichiometry, which confirms that Sn is mainly present as Sn(II).

^{13}C MAS-NMR spectra for 0D-[$TEASnCl_3$][TEACl] (Fig. S5, ESI†) do not show any diminution in the signal's intensity, such as 0D-TEA_4SnBr_6 compounds, so π-stacking is negligible.[51] In Fig. S3 and Table S3 (ESI†), multiple displacements are observed in the PL wavelength of the 0D-[$TEASnCl_3$][TEACl] microcrystal, between 630 nm for [TEA]/[Sn^{2+}] = 1 and 595 nm for [TEA]/[Sn^{2+}] = 2. This displacement may be due to tilting of the $[SnCl_3]^-$ tetrahedra induced by the increase in TEA^+ concentration.[56] The increase in the PLQY of 0D-TEA-based tin(II) chloride synthesized at a [TEA]/[Sn^{2+}] ratio between 2 and 4, and the reflections related to TEACl could suggest the formation of [$TEASnCl_3$][$TEACl]_X$ (where X is the number of TEACl molecules associated with the principal structure $TEASnCl_3$).[55]

In the synthesis of TEA-based Sn(II) iodide, only pure 2D-TEA_2SnI_4 microcrystals were predominantly obtained at all the explored molar ratios (Fig. S7, ESI†), without any evidence of dimensionality change. The XRD diffraction pattern shows multiple peaks at 5.53°, 11.23°, 16.98°, 22.73°, and 28.53° and separated by a period of ∼5.7° (Fig. S7, ESI†), which indicates the formation of the Ruddlesden–Popper phase for 2D-TEA_2SnI_4.[46] These could be confirmed with EDS analysis shown in Table S1 (ESI†). The absence of peaks was observed in the XRD patterns of 0D TEA-based tin(II) iodide. PL and PLE spectra (Fig. S7 and Table S3, ESI†) of TEA-based Sn(II) iodide display similar results for all the [TEA]/[Sn^{2+}] ratios tested. PLE and PL spectra are composed of a narrow band at 620 nm and 660 nm, respectively, and a small Stokes shift of around 80 meV, which is characteristic of radiative recombination of free excitons. The PLQY for 2D-TEA_2SnI_4 microcrystals (Table S3, ESI†) obtained in this work is relatively low (PLQY = 3%) compared with the record value reported by other authors (18.85% for nanodisk solution in *n*-hexane[46] and 23% in thin films[63]). This suggested the formation of multiple native superficial defects such as Sn(II) vacancies that affect the emissive properties of 2D-TEA_2SnI_4 microcrystals, as observed on different metal–organic and inorganic tin(II) halide nanocrystals synthesized by the hot injection method.[63,64]

Conclusions

In summary, the hot injection approach has proven to be an optimal platform to explore the dimensionality modulation in lead-free perovskites. Different low dimensionality 0D and 2D microplates based on 2-thiopheneethylammonium tin(II) bromide were successfully synthesized at 160 °C in low-polarity solvents. Experiments conducted at different molar ratios of precursors showed the possibility of modulating the dimensionality of 2D-TEA_2SnBr_4 microplates into 0D-TEA_4SnBr_6 with an increase of TEA molarity in solution, giving access to an orange light lead-free material with a PL emission at 610 nm, a strong Stokes shift of 2.3 eV and a high PLQY of 75% in thin films.

A similar dimensional transition was not observable for 0D-[$TEASnCl_3$][TEACl] and 2D-TEA_2SnI_4. It is worth noting that 0D-[$TEASnCl_3$][TEACl] showed good optical properties with a maximum PLQY of 25%. The PLQY of 0D-TEA_4SnBr_6 is higher than those of 0D-[$TEASnCl_3$][TEACl] and 2D-TEA_2SnI_4 because of the confinement effects and separation between inorganic moieties. Although the superior PLQYs for 0D-TEA_4SnBr_6 and 0D-[$TEASnCl_3$][TEACl] are related to the recombination of self-trapped excitons, the first of them exhibited a higher stable PL emission compared to its chloride analogue. This dimensional modulation can be a useful approach to obtain and design high luminescent lead-free materials with interesting properties for practical applications.

Conflicts of interest

There are no conflicts to declare.

Acknowledgements

This project has received funding from the European Union's Horizon 2020 research and innovation program under grant agreement No. 862656 (project DROP-IT) by the Spanish MICINN through project no. PID2020-120484RB. We acknowledge the support from the Spanish MINECO through the project Nirvana (no. PID2020-119628RB-C31) by MCIN/AEI/10.13039/501100011033. Also, we acknowledge the financial support from Generalitat Valenciana through the CIDEGENT contract (ref: CIDEGENT/2021/044) and CIAPOS 2022/018 grant. The work was partially funded by MCIN/AEI through project TED2021-131600B-C32.

References

1 E. Aydin, T. G. Allen, M. De Bastiani, A. Razzaq, L. Xu, E. Ugur, J. Liu and S. De Wolf, Pathways toward commercial perovskite/silicon tandem photovoltaics, *Science*, 2024, **383**, eadh3849.
2 M. Pitaro, E. K. Tekelenburg, S. Shao and M. A. Loi, Tin Halide Perovskites: From Fundamental Properties to Solar Cells, *Adv. Mater.*, 2022, **34**, 2105844.
3 M. Malekshahi Byranvand, W. Zuo, R. Imani, M. Pazoki and M. Saliba, Tin-based halide perovskite materials: properties and applications, *Chem. Sci.*, 2022, **13**, 6766.
4 M. Awais, R. L. Kirsch, V. Yeddu and M. I. Saidaminov, Tin Halide Perovskites Going Forward: Frost Diagrams Offer Hints, *ACS Mater. Lett.*, 2021, **3**, 299–307.
5 Y. Lin, Y. Bai, Y. Fang, Q. Wang, Y. Deng and J. Huang, Suppressed Ion Migration in Low-Dimensional Perovskites, *ACS Energy Lett.*, 2017, **2**, 1571–1572.
6 S. Ghimire and C. Klinke, Two-dimensional halide perovskites: synthesis, optoelectronic properties, stability, and applications, *Nanoscale*, 2021, **13**, 12394.
7 B. Su, G. Song, M. S. Molokeev, Z. Lin and Z. Xia, Synthesis, Crystal Structure and Green Luminescence in Zero-Dimensional Tin Halide $(C_8H_{14}N_2)_2SnBr_6$, *Inorg. Chem.*, 2020, **59**, 9962–9968.
8 L. Mao, C. C. Stoumpos and M. G. Kanatzidis, Two-Dimensional Hybrid Halide Perovskites: Principles and Promises, *ACS Energy Lett.*, 2018, **3**, 54–62.
9 Y. Chen, Y. Sun, J. Peng, J. Tang, K. Zheng and Z. Liang, 2D Ruddlesden–Popper Perovskites for Optoelectronics, *Adv. Mater.*, 2018, **30**, 1703487.
10 J. Hu, L. Yan and W. You, Two-Dimensional Organic–Inorganic Hybrid Perovskites: A New Platform for Optoelectronic Applications, *Adv. Mater.*, 2018, **30**, 1802041.
11 D. B. Straus and C. R. Kagan, Electrons, Excitons, and Phonons in Two-Dimensional Hybrid Perovskites: Connecting Structural, Optical, and Electronic Properties, *J. Phys. Chem. Lett.*, 2018, **9**, 1434–1447.
12 M. G. Ju, J. Dai, L. Ma, Y. Zhou and X. C. Zeng, Zero-Dimensional Organic−Inorganic Perovskite Variant: Transition between Molecular and Solid Crystal, *J. Am. Chem. Soc.*, 2018, **140**, 10456–10463.
13 B. M. Benin, D. N. Dirin, V. Morad, M. Wçrle, S. Yakunin, G. Rainm, O. Nazarenko, M. Fischer, I. Infante and M. V. Kovalenko, Highly Emissive Self-Trapped Excitons in Fully Inorganic Zero- Dimensional Tin Halides, *Angew. Chem., Int. Ed.*, 2018, **57**, 11329–11333.
14 H. Shi, D. Han, B. Saparov, Y. Z. Ma, S. Chen, W. Ming, C. Zhou, B. Ma and M. H. Du, Unraveling luminescence mechanisms in zero-dimensional halide perovskites, *J. Mater. Chem. C*, 2018, **6**, 6398.
15 J. Yin, P. Maity, M. De Bastiani, I. Dursun, O. M. Bakr, J. L. Brédas and O. F. Mohammed, Molecular behavior of zero-dimensional perovskites, *Sci. Adv.*, 2017, **3**, e1701793.
16 S. Seth and A. Samanta Photoluminescence, of Zero-Dimensional Perovskites and Perovskite-Related Materials, *J. Phys. Chem. Lett.*, 2018, **9**, 176–183.
17 J. L. Wardell, Tin: Inorganic Chemistry, in *Encyclopedia of Inorganic and Bioinorganic Chemistry*, ed. R. A. Scott, 2011.
18 J. D. Donaldson and S. M. Grimes, in *The inorganic chemistry of tin, Chemistry of Tin*, ed. P. J. Smith, Springer, Dordrecht, 1998.
19 H. Peng, X. Wang, Z. Zhang, Y. Tian, Y. Xiao, J. Hu, J. Wang and B. Zou, Bulk assembly of a 0D organic tin(II) chloride hybrid with high anti-water stability, *Chem. Commun.*, 2021, **57**, 8162.
20 D. J. Kubicki, D. Prochowicz, E. Salager, A. Rakhmatullin, C. P. Grey, L. Emsley and S. D. Stranks, Local Structure and Dynamics in Methylammonium, Formamidinium, and Cesium Tin (II) Mixed-Halide Perovskites from ^{119}Sn Solid-State NMR, *J. Am. Chem. Soc.*, 2020, **142**, 7813–7826.
21 Y. Lin, Y. Zhong, Y. Lin, J. Lin, L. Pang, Z. Zhang, Y. Zhao, X. Y. Huang and K. Z. Du, White light emission in 0D halide perovskite $[(CH_3)_3S]_2SnCl_6{\cdot}H_2O$ crystals through variation of doping ns^2 ions, *Front. Optoelectron.*, 2024, **17**, 6.
22 K. Tao, Q. Li and Q. Yan, 1D Tin (II)-Based Chiral Hybrid Perovskite Single Crystals with Extremely Distorted Inorganic Chains for Second Harmonic Generation, *Adv. Opt. Mater.*, 2024, 2400018.
23 Y. Dang, Y. Zhou, X. Liu, D. Ju, S. Xia, H. Xia and X. Tao, Formation of Hybrid Perovskite Tin Iodide Single Crystals by Top-Seeded Solution Growth, *Angew. Chem., Int. Ed.*, 2016, **55**, 3447–3450.
24 Y. Ju, X. Wu, S. Huang, G. Dai, T. Song and H. Zhong, The Evolution of Photoluminescence Properties of PEA_2SnI_4 Upon Oxygen Exposure: Insight into Concentration Effects, *Adv. Funct. Mater.*, 2022, **32**, 2108296.
25 J. N. Lv, J. Zhang, Y. M. Liu, S. Y. Zhang, X. Y. Deng, M. Xu, X. W. Lei, Z. W. Chen and C. Y. Yue, Zero-dimensional hybrid tin halides with stable broadband light emissions, *Dalton Trans.*, 2024, **53**, 4698.
26 D. S. Zheng, S. B. Xiao, H. J. Yang, Z. Deng, L. J. Xu and Z. N. Chen, *J. Lumin.*, 2024, **270**, 120530.
27 S. Bonomi, M. Patrini, G. Bongiovanni and L. Malavasi, Versatile vapor phase deposition approach to cesium tin bromide materials $CsSnBr_3$, $CsSn_2Br_5$ and Cs_2SnBr_6, *RSC Adv.*, 2020, **10**, 28478.
28 I. Spanopoulos, I. Hadar, W. Ke, P. Guo, S. Sidhik, M. Kepenekian, J. Even, A. D. Mohite, R. D. Schaller and

M. G. Kanatzidis, Water- Stable 1D Hybrid Tin(II) Iodide Emits Broad Light with 36% Photoluminescence Quantum Efficiency, *J. Am. Chem. Soc.*, 2020, **142**, 9028–9038.

29 C. C. Stoumpos, L. Mao, C. D. Malliakas and M. G. Kanatzidis, Structure–Band Gap Relationships in Hexagonal Polytypes and Low-Dimensional Structures of Hybrid Tin Iodide Perovskites, *Inorg. Chem.*, 2017, **56**, 56–73.

30 Y. E. Ajjouri, F. Locardi, M. C. Gélvez-Rueda, M. Prato, M. Sessolo, M. Ferretti, F. C. Grozema, F. Palazon and H. J. Bolink, Mechanochemical Synthesis of Sn(II) and Sn(IV) Iodide Perovskites and Study of Their Structural, Chemical, Thermal, Optical, and Electrical Properties, *Energy Technol.*, 2020, **8**, 1900788.

31 G. Schileo and G. Grancini, Lead or no lead? Availability, toxicity, sustainability and environmental impact of lead-free perovskite solar cells, *J. Mater. Chem. C*, 2021, **9**, 67.

32 P. Zhu and J. Zhu, Low-dimensional metal halide perovskites and related optoelectronic applications, *InfoMat*, 2020, **2**, 341–378.

33 C. Ortiz- Cervantes, P. Carmona- Monroy and D. Solis-Ibarra, Two-Dimensional Halide Perovskites in Solar Cells: 2D or not 2D?, *ChemSusChem*, 2019, **12**, 1560–1575.

34 Y. Du, D. Zhu, Q. Cai, S. Yuan, G. Shen, P. Dong, C. Mu, Y. Wang and X. C. Ai, Spacer Engineering of Thiophene-Based Two-Dimensional/Three-Dimensional Hybrid Perovskites for Stable and Efficient Solar Cells, *J. Phys. Chem. C*, 2022, **126**, 3351–3358.

35 K. C. Hsiao, M. H. Jao, B. T. Li, T. H. Lin, S. H. C. Liao, M. C. Wu and W. F. Su, Enhancing Efficiency and Stability of Hot Casting p–i–n Perovskite Solar Cell *via* Dipolar Ion Passivation, *ACS Appl. Energy Mater.*, 2019, **2**, 4821–4832.

36 J. T. Lin, D. G. Chen, C. H. Wu, C. S. Hsu, C. Y. Chien, H. M. Chen, P. T. Chou and C. W. Chiu, A Universal Approach for Controllable Synthesis of n-Specific Layered 2D Perovskite Nanoplates, *Angew. Chem., Int. Ed.*, 2021, **60**, 7866–7872.

37 H. Jia, H. Shi, R. Yu, H. Ma, Z. Wang, C. Zou and Z. Tan, Biuret Induced Tin-Anchoring and Crystallization Regulating for Efficient Lead-Free Tin Halide Perovskite Light-Emitting Diodes, *Small*, 2022, **18**, 2200036.

38 G. Ding, X. He, H. Zhang and H. Fu, Ethanol-assisted synthesis of two-dimensional tin (II) halide perovskite single crystals for amplified spontaneous emission, *J. Mater. Chem. C*, 2022, **10**, 10902–10907.

39 L. Protesescu, S. Yakunin, M. I. Bodnarchuk, F. Krieg, R. Caputo, C. H. Hendon, R. X. Yang, A. Walsh and M. V. Kovalenko, Nanocrystals of Cesium Lead Halide Perovskites ($CsPbX_3$, X = Cl, Br, and I): Novel Optoelectronic Materials Showing Bright Emission with Wide Color Gamut, *Nano Lett.*, 2015, **15**, 3692–3696.

40 Q. A. Akkerman, S. G. Motti, A. R. Srimath Kandada, E. Mosconi, V. D'Innocenzo, G. Bertoni, S. Marras, B. A. Kamino, L. Miranda, F. De Angelis, A. Petrozza, M. Prato and L. Manna, Solution Synthesis Approach to Colloidal Cesium Lead Halide Perovskite Nanoplatelets with Monolayer-Level Thickness Control, *J. Am. Chem. Soc.*, 2016, **138**, 1010–1016.

41 A. Pan, B. He, X. Fan, Z. Liu, J. J. Urban, A. P. Alivisatos, L. He and Y. Liu, Insight into the Ligand-Mediated Synthesis of Colloidal $CsPbBr_3$ Perovskite Nanocrystals: The Role of Organic Acid, Base, and Cesium Precursors, *ACS Nano*, 2016, **10**, 7943–7954.

42 K. M. McCall, V. Morad, B. M. Benin and M. V. Kovalenko, Efficient Lone-Pair-Driven Luminescence: Structure–Property Relationships in Emissive $5s^2$ Metal Halides, *ACS Mater. Lett.*, 2020, **2**(9), 1218–1232.

43 R. Chiara, Y. O. Ciftci, V. I. E. Queloz, M. K. Nazeeruddin, G. Grancini and L. Malavasi, Green-Emitting Lead-Free Cs_4SnBr_6 Zero-Dimensional Perovskite Nanocrystals with Improved Air Stability, *J. Phys. Chem. Lett.*, 2020, **11**, 618–623.

44 T. C. Jellicoe, J. M. Richter, H. F. J. Glass, M. Tabachnyk, R. Brady, S. E. Dutton, A. Rao, R. H. Friend, D. Credgington, N. C. Greenham and M. L. Böhm, Synthesis and Optical Properties of Lead-Free Cesium Tin Halide Perovskite Nanocrystals, *J. Am. Chem. Soc.*, 2016, **138**, 2941–2944.

45 M. Wang, J. Tang, H. Wang, C. Zhang, Y. S. Zhao and J. Yao, Grain Boundary Enhanced Photoluminescence Anisotropy in Two-Dimensional Hybrid Perovskite Films, *Adv. Optical Mater.*, 2020, **8**, 1901780.

46 J. T. Lin, C. C. Liao, C. S. Hsu, D. G. Chen, H. M. Chen, M. K. Tsai, P. T. Chou and C. W. Chiu, Harnessing Dielectric Confinement on Tin Perovskites to Achieve Emission Quantum Yield up to 21%, *J. Am. Chem. Soc.*, 2019, **141**, 10324–10330.

47 J. Almutlaq, J. Yin, O. F. Mohammed and O. M. Bakr, The Benefit and Challenges of Zero-Dimensional Perovskites, *J. Phys. Chem. Lett.*, 2018, **9**(14), 4131–4138.

48 S. Seth and A. Samanta Photoluminescence, of Zero-Dimensional Perovskites and Perovskite-Related Materials, *J. Phys. Chem. Lett.*, 2018, **9**(1), 176–183.

49 L. J. Xu, H. Lin, S. Lee, C. Zhou, M. Worku, M. Chaaban, Q. He, A. Plaviak, X. Lin, B. Chen, M. H. Du and B. Ma, 0D and 2D: The Cases of Phenylethylammonium Tin Bromide Hybrids, *Chem. Mater.*, 2020, **32**, 4692–4698.

50 J. C. Dahl, S. Niblett, Y. Cho, X. Wang, Y. Zhang, E. M. Chan and A. Paul Alivisatos, Scientific Machine Learning of 2D Perovskite Nanosheet Formation, *J. Am. Chem. Soc.*, 2023, **145**(42), 23076–23087.

51 T. Sheikh, S. Maqbool, P. Mandal and A. Nag, Introducing Intermolecular Cation-p Interactions for Water-Stable Low Dimensional Hybrid Lead Halide Perovskites, *Angew. Chem., Int. Ed.*, 2021, **60**, 18265–18271.

52 J. Wang, J. Dong, F. Lu, C. Sun, Q. Zhang. and N. Wang, Two-dimensional lead-free halide perovskite materials and devices, *J. Mater. Chem. A*, 2019, **7**, 23563.

53 L. Zhang, Z. Luo, W. Wang, Y. Liu, X. He and Z. Quan, Organic Cation-Directed Modulation of Emissions in Zero-Dimensional Hybrid Tin Bromides, *Inorg. Chem.*, 2022, **61**(37), 14857–14863.

54 M. Roknuzzaman, K. Ostrikov, H. Wang, A. Du and T. Tesfamichael, Towards lead-free perovskite photovoltaics

and optoelectronics by *ab-initio* simulations, *Sci. Rep.*, 2017, **7**, 14025.

55 X. Liu, Y. Li, T. Liang and J. Fan, Role of Polyhedron Unit in Distinct Photophysics of Zero Dimensional Organic– Inorganic Hybrid Tin Halide Compounds, *J. Phys. Chem. Lett.*, 2021, **12**, 5765–5773.

56 M. Ha, A. Karmakar, G. M. Bernard, E. Basilio, A. Krishnamurthy, A. M. Askar, K. Shankar, S. Kroeker and V. K. Michaelis, Phase Evolution in Methylammonium Tin Halide Perovskites with Variable Temperature Solid-State ^{119}Sn NMR Spectroscopy, *J. Phys. Chem. C*, 2020, **124**, 15015–15027.

57 M. M. Elsenety, A. Kaltzoglou, I. Koutselas, V. Psycharis, C. P. Raptopoulou, A. G. Kontos, K. G. Papadokostaki, N. K. Nasikas and P. Falaras, Synthesis, Crystal Structure, and Broadband Emission of $(CH_3)_3SSnCl_3$, *Inorg. Chem.*, 2022, **61**, 4769–4777.

58 X. Liu, W. Wu, Y. Zhang, Y. Li, H. Wu and J. Fan, Critical Roles of High- and Low-Frequency Optical Phonons in Photodynamics of Zero-Dimensional Perovskite-like $(C_6H_{22}N_4Cl_3)SnCl_3$ Crystals, *J. Phys. Chem. Lett.*, 2019, **10**, 7586–7593.

59 A. Karmakar, S. Mukhopadhyay, P. G. B. Gachod, V. A. Mora-Gomez, G. M. Bernard, A. Brown and V. K. Michaelis, Uncovering Halogen Mixing and Octahedral Dynamics in Cs_2SnX_6 by Multinuclear Magnetic Resonance Spectroscopy, *Chem. Mater.*, 2021, **33**, 6078–6090.

60 A. Kaiba, M. H. Geesi, Y. Riadi, E. O. Ibnouf, T. A. Aljohani and P. Guionneau, A new Organic–Inorganic hybrid compound $(NH_3(CH_2)_2C_6H_5)_2[SnCl_6]$: Crystal structure, characterization, Hirshfeld surface analysis, DFT calculation, vibrational properties, and biological evaluation, *J. Solid-State Chem.*, 2021, **304**, 122587.

61 J. Li, Z. Tan, M. Hu, C. Chen, J. Luo, S. Li, L. Gao, Z. Xiao, G. Niu and J. Tang, Antimony doped Cs_2SnCl_6 with bright and stable emission, *Front. Optoelectron.*, 2019, **12**(4), 352–364.

62 A. Karmakar, A. Bhattacharya, D. Sarkar, G. M. Bernard, A. Mar and V. K. Michaelis, Influence of hidden halogen mobility on local structure of $CsSn(Cl_{1-x}Br_x)_3$ mixed-halide perovskites by solid-state NMR, *Chem. Sci.*, 2021, **12**, 3253.

63 J. T. Lin, Y. K. Hu, C. H. Hou, C. C. Liao, W. T. Chuang, C. W. Chiu, M. K. Tsai, J. J. Shyue and P. T. Chou, Superior Stability and Emission Quantum Yield (23% ± 3%) of Single-Layer 2D Tin Perovskite TEA_2SnI_4 via Thiocyanate Passivation, *Small*, 2020, **16**, 2000903.

64 Q. Liu, J. Yin, B. B. Zhang, J. K. Chen, Y. Zhou, L. M. Zhang, L. M. Wang, Q. Zhao, J. Hou, J. Shu, B. Song, N. Shirahata, O. M. Bakr, O. F. Mohammed and H. T. Sun, Theory-Guided Synthesis of Highly Luminescent Colloidal Cesium Tin Halide Perovskite Nanocrystals, *J. Am. Chem. Soc.*, 2021, **143**, 5470–5480.

